8.5 Modeling of Irradiation Hardening of Iron After Low Dose and Low Temperature Neutron Irradiation — X. Hu, D. Xu, B. D. Wirth (University of Tennessee, Knoxville), and T. S. Byun (Oak Ridge National Laboratory)

OBJECTIVE

The objective of this work is to model the yield strength increase of iron after low dose and low temperature neutron irradiation and to provide insight into the underlying microstructure – property relationships.

SUMMARY

Irradiation hardening is a prominent low temperature degradation phenomena in materials. In this paper, a reaction-diffusion cluster dynamics model is used to predict the distribution of vacancy and interstitial clusters in iron subject to low temperature (< 373K) and low dose (< 0.1 dpa) neutron irradiation. The predicted microstructure evolutions of high purity iron samples are compared to positron annihilation spectroscopy (PAS) and transmission electron microscopy (TEM) observations and show good agreement for neutron irradiation in this regime. The defect cluster distributions are then coupled to a dispersed barrier hardening model that assumes a strength factor, α, which varies with cluster type and size to compute the yield strength increase, the results of which are compared to the values obtained from tensile tests. A reasonable agreement between modeling and experiments is achieved.

PROGRESS AND STATUS

Introduction

Exposure of metallic structural materials to irradiation environments results in significant performance degradation, which limits the extended operation of current generation light water reactors and restricts the design of advanced fission and fusion reactors [1-4]. Irradiation hardening is the most prevailing degradation phenomena at low temperature ($T_{irr} < 0.3\ T_m$), routinely characterized by an increase of yield strength and decrease in uniform ductility in tension tests, and results from the accumulation of various irradiation-produced defects, e.g., defect clusters, impurity-defect cluster complexes, dislocation loops and lines, voids, bubbles and precipitates [5, 6]. The existence of these defects impedes dislocation glide during deformation, causing the increase of yield strength, which is almost always accompanied by degradation of other critical mechanical properties such as the loss of ductility resulting in embrittlement [7-11].

The problem of irradiation hardening has been investigated both experimentally and theoretically in considerable depth since the 1960s [9-27]. In experimental studies, the irradiation hardening behavior of body-centered cubic (BCC), face-centered cubic (FCC), and hexagonal close-packed (HCP) alloys and pure metals has been thoroughly investigated following neutron, spallation proton and ion irradiation at low temperatures by many researchers [12-19], which aimed to characterize the dose dependence of irradiation hardening and explain the results with respect to the plastic deformation and defect-cluster accumulation behaviors. For example, Byun and Farrell [18] examined the irradiation behavior of 19 polycrystalline metals after low temperature irradiation,

indicating the transition between the low-dose and high-dose regimes, and elucidated the relationship among irradiation hardening, plastic instability, deformation mechanism, and defect-cluster number density. Rice and Zinkle [19] correlated the TEM observed dislocation loop distributions to the yield stress increase of neutron irradiated vanadium alloys to study the barrier strength.

A great deal of effort has been made to reveal the mechanisms of irradiation hardening in metals due to the various irradiation-produced defects. The mechanical behavior of irradiated metals is routinely correlated to the observed microstructure by use of either a dispersed barrier-hardening model [20, 21, 22], a cascade-induced source hardening model [9,12], or a dislocation density-based constitutive model [23].

The dispersed barrier-hardening model is commonly used to correlate yield strength increases to the irradiation-produced defects. Although there are multiple hypotheses to correlate the change in yield strength with the number density and size of defects, the dose-dependence of the yield stress, $\Delta\sigma_{YS}$, has been frequently explored using an Orowan strength model associated with the assumption that dislocation bypass of impenetrable obstacles occurs by bowing around them. Based on Orowan's model, the most commonly used expression for the change in shear stress, $\Delta\tau_s$, induced in the dislocation glide plane by a regular array of defects is:

$$\Delta\tau_s = \alpha\mu b(Nd)^{1/2} \tag{1}$$

where μ is the shear modulus of the matrix, *b* the magnitude of the dislocation Burgers vector, *N* the defect number density, and *d* is the defect diameter. In this formulation, the square-root factor represents the reciprocal of the average distance between obstacles. The α factor is typically referred to as the 'barrier strength', and accounts for the fact that some obstacles may be partially cut or sheared by the dislocation as it bows out during the glide process, with a resistance less than an impenetrable Orowan obstacle (α =1).

The cascade-induced source hardening model proposed by Singh [9] is based on the idea that the experimentally observed yield drop results from the unlocking of grown-in matrix dislocations decorated by self-interstitial dislocation loops. In order to initiate plastic deformation in materials, these dislocations act as Frank-Read dislocation sources. Consequently, the stress necessary to unlock the dislocations represents the upper yield stress, which has different expressions for two distinct cases: (i) the loops are clearly separated by distances similar to their size, and (ii) the loops are no longer well separated but form a network. The expressions of upper yield stress for these two cases are provided in Eq. (2) and (3), respectively.

$$\tau = 0.1\mu(b/l)(d/y)^2 \tag{2}$$

and

$$\tau = \mu b / 8\pi(1-\nu)y \tag{3}$$

where *l* is the average spacing of dislocation loops, and *y* is the distance between the straight row of sessile dislocation loops and the straight glide dislocation. However, this model does not adequately describe the dose dependence of hardening [24].

A dislocation density-based constitutive model successfully reproduced the post-yield deformation behavior of irradiated Cu tested in uniaxial tension at low to intermediate homologous temperature, based on information from molecular dynamic simulations of the interaction behavior between gliding dislocations and radiation-induced stacking fault tetrahedra [23]. This isotropic internal state variable plasticity model included mechanisms for dislocation density growth and multiplication, as well as for irradiation-induced defect density evolution as a result of dislocation interactions. The final coarse-grained model was implemented into a finite element framework and used to simulate the behavior of tensile specimens with varying levels of irradiation-induced material damage.

Despite extensive effort to investigate the irradiation hardening behavior through both experimental and modeling techniques, a self-consistent and complete model validated by experimental results is not yet available to bridge the irradiation-produced microstructure evolutions with the resulting hardening behavior. In this paper, neutron irradiation induced hardening of iron samples is taken as an example to demonstrate the quantitative influence of defect distribution on the increase of yield strength. Among the above-mentioned models, the dispersed barrier-hardening model is most commonly used to predict the yield strength increase, due to its explicit relationship with the irradiation-induced defect information. For the dispersed barrier model, it is noted that attempts to correlate irradiation-produced microstructural evolution with changes in mechanical properties rely on a well-established theory to compute the resolved shear stress required to move dislocations through a field of obstacles. Various modifications to the Orowan equation have been proposed [11, 25]. Similar to Equation (1), these efforts have focused on finding more accurate correlations between the resolved shear stress and the number density and size of the irradiation-produced defects. The comparisons of the yield strength increase computed using this model and the corresponding experimental measurements have been carried out for different structural materials, such as 304 and 316 stainless steels [26] and ferritic steels [27]. In these studies, a rough estimation of the defect cluster density was used such that the defect accumulation behavior was assumed linear at very low doses (less than 0.0001 dpa) and proportional to the square root of dose at higher doses. However, an accurate estimation of the yield strength increase requires a precise prediction of the defect distribution in the material under irradiation.

Cluster dynamics has proved to be a useful technique to simulate microstructure evolution under irradiation. For example, Xu et al., [28-30] developed a spatially dependent cluster dynamics model based on reaction-diffusion rate theory to study the nanoscale microstructural evolution of keV helium-implanted iron and 1 MeV krypton-irradiated-molybdenum. Hu et al., [31,32] also applied the same model to study the helium – point defect interactions in helium-implanted single crystalline iron. In addition, other researchers [33, 34] have made improvements to the computing efficiency of the cluster dynamics model and applied this method to various ion irradiation conditions. However, a limited number of papers exist in the literature [35] that utilizes the cluster dynamics model-to-model neutron irradiation experiments. The difficulty of neutron irradiation damage modeling arises from the need for an accurate estimation of the primary knock-on atoms induced by neutron scattering across a broad energy spectrum. A cluster dynamics model based on the reaction-diffusion rate theory is applied here to simulate the neutron irradiation induced microstructure evolution in BCC iron, which provides radiation-induced defect concentrations for the hardening model.

The objective of this study is, therefore, to introduce a coupled modeling and experimental study by applying the experimentally validated (i.e., PAS and TEM) cluster dynamics modeling results of the defect evolution in iron under neutron irradiation to a dispersed barrier irradiation-hardening model. The results presented here favorably compare to tensile test measurements of iron samples, and provide insights into the underlying microstructure-property relationships.

Experiment

In the present study, microstructural and mechanical properties of two different high purity polycrystalline iron samples are investigated after neutron irradiation. The chemical compositions of the samples and their pre-irradiation heat treatments are shown in Table 1. Fast neutron irradiation experiments were conducted in the hydraulic tube facility of the High Flux Isotope Reactor (HFIR) at Oak Ridge National Laboratory. Eldrup etc. [36] examined the microstructures of the Fe-a samples after neutron irradiation using PAS and TEM. The positron lifetime measurements were performed to obtain information on vacancy cluster distribution while the interstitial cluster density was determined by TEM observation [36]. Tensile tests were performed for both the Fe-a and Fe-b specimens at room temperature in screw-driven machines at a nominal strain rate of about 10^{-3} s^{-1}. The neutron irradiation and testing conditions, and baseline tensile data of these two samples are listed in Table 1. The present paper will focus on modeling work to compare to the experiment observations presented in Section 4, and thus many of the specific details of the experiments are not described here; additional details are available in References [18, 36-39].

Table 1. Chemical compositions, heat treatment, irradiation conditions, testing conditions, and baseline tensile data of the two types of iron samples.

	Fe-a	Fe-b
Chemical compostition (wt%)	99.995% purity	Fe-0.013C-0.018Mn-0.018Ni (99.94% purity)
Heat treatment in vacuum	Annealed at 873 K for 1 h	Annealed at 873 K for 1 h
Crystal structure	BCC	BCC
Tensile test temperature (K)	Room Temperature	Room Temperature
Yield stress (MPa at 0 dpa)	104	213
Uniform elongation (0 dpa)	0.26	0.29
Dose range (dpa)	0-0.79	0-1.07
Irradiation temperature (K)	333-373	333-373

Modeling

Cluster dynamics model based on reaction-diffusion rate theory

Free vacancies and self-interstitial atoms (SIAs), as well as spherical vacancy clusters and SIA clusters in the form of planar, prismatic dislocation loops are continuously formed and will evolve in pure body-centered cubic iron under neutron irradiation [40, 41, 42]. A cluster dynamics model based on the reaction-diffusion rate theory is used here to predict the evolution of the defect clusters, which is a modified version of the model developed by Xu and Wirth [28, 29, 30, 40] and only considers the intrinsic defects and their clusters. Furthermore, since the probability that SIA and vacancy co-exist in a single cluster is very low due to their strong tendency for recombination, no mixed I-V clusters were considered, and it is thus sufficient to define any cluster using just an integer, with its absolute value being the number of point defects contained in the complexes and its sign ('−' for SIA clusters, or '+' for V-clusters) indicating the character of the cluster. Two numbers, NI and NV, are chosen as the number of interstitials in the largest SIA-cluster, and the number of vacancies in the largest V-cluster, respectively. Physically, these numbers prescribe the 'phase space' within which the clusters can interact with each other, and ensure the conservation of point defects. NI and NV should be chosen large enough so that the computational results are not impacted by a prescribed phase space that is too small (e.g., insufficient cluster size to allow growth to large defect cluster size). Note that a spatially dependent defect generation in metals occurs under ion implantations, and therefore was necessarily taken into account in the previous modeling effort [28-32, 40]. However, the nature of defect generation in metals induced by ions and neutrons is significantly different. Since the energy transfer cross section for ions is an atomic cross section (~ 10^{-17} cm^2) while that for neutrons is a nuclear cross section (~10^{-24} cm^2), neutrons have a much larger range when travelling in a material than an ion does. The damage production varies weakly along the depth direction for neutron irradiation and therefore, it is reasonable to treat the distribution of radiation damage production as homogeneous. Thus an explicit spatial dimension is no longer necessary in this model, different from the model introduced in Reference [40], at least for low neutron dose levels before a clear spatial correlation of the defect microstructure develops.

Since there is no spatial dependence, the concentration of each cluster is only a function of time, and ordinary differential equations are employed to describe the defect evolution. The binary reactions discussed in References. [28-32, 40-42] are still appropriate and become simpler, because there are only two types of defects (V- and SIA-clusters) considered during neutron irradiation. The generic form to describe the evolution of a cluster is:

$$\frac{dC_i}{dt} = \phi \times P_i + G_T + G_E - A_T - A_E \ , \tag{4}$$

where C_i refers to the volumetric concentration (in $1/m^3$) of the i-th cluster, ϕ is neutron flux (in neutron/m^2/sec), P_i is the production 'probability' of the i-th cluster by neutron irradiation, *G* refers to the collective generation rates, *A* indicates the collective annihilation rates, *T* refers to generation or annihilation by trapping events, and *E* refers

to generation or annihilation by emission events. The detailed construction of the coupled system of ODEs is thus (for which $\Lambda = \lfloor -NI, NV \rfloor$ is the prescribed phase space):

$$\frac{dC_i}{dt} = \phi \times P_i + \sum_{\substack{m+p=i \\ m,p\neq 0 \\ m.p\in\Lambda}} k^+_{m,p} C_m C_P - \sum_{\substack{m\neq i \\ m\neq 0 \\ m.m+i\in\Lambda}} k^+_{m,i} C_m C_i - k^-_i C_i \tag{5}$$

for i=NV or –NI, and

$$\frac{dC_i}{dt} = \phi \times P_i + \sum_{\substack{m+p=i \\ m,p\neq 0 \\ m.p\in\Lambda}} k^+_{m,p} C_m C_P + k^-_{i+1} C_{i+1} - \sum_{\substack{m\neq i \\ m\neq 0 \\ m.m+i\in\Lambda}} k^+_{m,i} C_m C_i - k^-_i C_i \tag{6}$$

for $\frac{NV}{2} < i < NV$, and

$$\frac{dC_i}{dt} = \phi \times P_i + \sum_{\substack{m+p=i \\ m,p\neq 0 \\ m.p\in\Lambda}} k^+_{m,p} C_m C_P + k^-_{i+1} C_{i+1} - \sum_{\substack{m\neq i \\ m\neq 0 \\ m.m+i\in\Lambda}} k^+_{m,i} C_m C_i - 2k^+_{i,i}\left(C_i\right)^2 - k^-_i C_i \tag{7}$$

for $2 \le i \le \frac{NV}{2}$, and

$$\frac{dC_i}{dt} = \phi \times P_i + \sum_{\substack{m+p=i \\ m,p\neq 0 \\ m.p\in\Lambda}} k^+_{m,p} C_m C_P + 2k^-_2 C_2 + \sum_{\substack{m>2 \\ m\in\Lambda}} k^-_m C_m - \sum_{\substack{m\neq i \\ m\neq 0 \\ m.m+i\in\Lambda}} k^+_{m,i} C_m C_i - 2k^+_{i,i}\left(C_i\right)^2 \tag{8}$$

for $i = 1$, and

$$\frac{dC_i}{dt} = \phi \times P_i + \sum_{\substack{m+p=i \\ m,p\neq 0 \\ m.p\in\Lambda}} k^+_{m,p} C_m C_P + 2k^-_{-2} C_{-2} + \sum_{\substack{m<-2 \\ m\in\Lambda}} k^-_m C_m - \sum_{\substack{m\neq i \\ m\neq 0 \\ m.m+i\in\Lambda}} k^+_{m,i} C_m C_i - 2k^+_{i,i}\left(C_i\right)^2 \tag{9}$$

for $i = -1$, and

$$\frac{dC_i}{dt} = \phi \times P_i + \sum_{\substack{m+p=i \\ m,p\neq 0 \\ m.p\in\Lambda}} k^+_{m,p} C_m C_P + k^-_{i-1} C_{i-1} - \sum_{\substack{m\neq i \\ m\neq 0 \\ m.m+i\in\Lambda}} k^+_{m,i} C_m C_i - 2k^+_{i,i}\left(C_i\right)^2 - k^-_i C_i \tag{10}$$

for $-\frac{NI}{2} \le i \le -2$, and

$$\frac{dC_i}{dt} = \phi \times P_i + \sum_{\substack{m+p=i \\ m,p\neq 0 \\ m.p\in\Lambda}} k^+_{m,p} C_m C_P + k^-_{i-1} C_{i-1} - \sum_{\substack{m\neq i \\ m\neq 0 \\ m.m+i\in\Lambda}} k^+_{m,i} C_m C_i - k^-_i C_i \tag{11}$$

for $-NI < i < -\frac{NI}{2}$, where k^+ is the forward reaction rate constant and k^- is the backward reaction rate constant, having the same expressions as the classic rate theory [41, 42], i.e.,

$$k^+_{m.p} = 4\pi(r_m + r_p)(D_m + D_p), \tag{12}$$

$$k^- = k^+ C_0 \exp\left(-\frac{E_b}{k_B T}\right), \tag{13}$$

where r_m and r_p are the trapping radii of clusters *m* and *p*, *D* is the diffusion coefficient of the reacting species, C_0 is the atomic number density of the iron matrix, E_b is the binding energy of a single point defect to the cluster, k_B is Boltzmann's constant, and *T* is the temperature. Note that for emission ($C \rightarrow A + B$), only those events in which at least one of the two products is a monomer (i.e., I or V) are considered since it is in general more energetically favorable for a cluster to emit a monomer than emit a dimer, trimer or multimer, which is consistent with previous models [28-30].

The external source of intrinsic point defects and the corresponding clusters is the neutron irradiation induced collision cascade occurring inside the iron samples exposed to the reactor environment. This generation term always exists during the neutron irradiation process and impacts the modeling results significantly, thus it is crucial to have an accurate predication of this damage production. In many previous cluster dynamic models [28, 29, 40, 41], the simple Frenkel pair point defect production mode has been applied without considering the generation of small defect clusters in displacement cascades. However, MD simulations [43-46] of cascades in BCC iron clearly show that energetic PKAs with kinetic energies greater than a few keV directly produce small interstitial and vacancy clusters rather than isolated Frenkel pairs. Xu et al. [40] discussed the applicability of Frenkel pair production versus intra-cascade cluster production in the modeling of 1 MeV krypton-ion irradiated molybdenum, concluding that the latter is the most applicable case. Therefore, here, intra-cascade cluster production is used to determine the defect production probability, P_i.

In our specific modeling of the neutron irradiation in HFIR, the PKA energy spectrum of neutron irradiation in iron was calculated by SPECTER [47, 48] (neutron damage calculations for materials under irradiations), the results of which are shown in Figure 1. The total displacements, created by the PKA were calculated using the Lindhard model [49], within which the kinetic energy, *T*, of a PKA is partitioned between electronic and nuclear stopping. The expression for the number of displacements is

$$\nu = \xi(T,Z)\left(\frac{T}{2E_d}\right), \tag{14}$$

where $\xi(T,Z)$ is a function of *T* and *Z* (atomic number), and is used to describe the part of the PKA kinetic energy that is available to generate atomic displacements by elastic collisions. E_d is the displacement energy , taken as the reference value of 40 eV for iron [43]. This partitioning coefficient is computed by

$$\xi(T,Z) = \frac{1}{1+0.134Z^{2/3}A^{-1/2}(3.4\varepsilon^{1/6}+0.4\varepsilon^{3/4}+\varepsilon)}, \tag{15}$$

$$\varepsilon = \frac{T}{2Z^2e^2/a}, \tag{16}$$

$$a = \frac{0.626a_{bohr}}{Z^{1/3}}, \tag{17}$$

where *A* is the atomic mass of the matrix element, a_{bohr} is Bohr radius, 0.529 Å, and $e^2 = 14.4$ eVÅ. Based on Equations (14) ~ (17), the total displacements (Frenkel pairs) can be calculated from the given PKA kinetic energy.

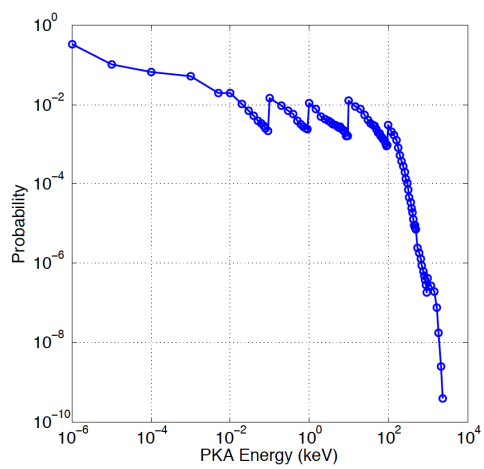

Figure 1. PKA spectrum in neutron irradiated iron in HFIR.

Xu et al., [40] summarized the fractions of total surviving point defects that are contained in small clusters I_1~I_{20} and V_1~V_9 and the surviving efficiency of point defects for four cascade energy intervals starting from 1 keV, based on analysis of an MD cascade simulation database in BCC iron that was provided by Stoller et al. [43]. The survival efficiency, *f*, refers to the number of interstitials and vacancies that survive the rapid recovery stage of cascade evolution in MD simulations, as well as following the initial cascade aging when the remaining mobile interstitial and vacancy clusters diffuse through and away from the vacancy rich core of the cascade. In the MD stage of cascade healing/in-cascade recombination, Stoller et al., [43] reported that this survival efficiency varies from one at low PKA energy to about 1/3 for PKA energies greater than 10 keV. Wirth and co-workers [50, 51] used kinetic Monte Carlo simulations to evaluate the additional recombination during the initial interstitial diffusion stage

following a cascade and observed sufficient recombination occurring to reduce this value to about 0.4 for low energy PKAs and further to about 0.12 for PKA energies of 20 keV and above.

Consequently, the survival of point defects in the cascade, $(\xi T / 2E_d) \times f$, will be partitioned into small clusters according to the clustering fractions obtained from this combination of MD simulations [43, 44] with an initial stage of cascade aging [50, 51]. For those PKAs with $\xi T < 1keV$, only individual Frenkel pairs, i.e., isolated I and V, were added in the amount $f\xi T / 2E_d$. The numbers of clusters produced by all PKA energies are then multiplied by the corresponding probabilities. The resulting cluster production 'probability' in unit of $1/PKA$ listed in Table 2.

Now it is necessary to determine the cluster production rate with respect to a specific neutron flux. This requires the PKA production rate be specified. From SPECTER calculations, the displacement cross section of the neutron irradiation is also provided, which enables computation of the total displacement rate (R_d) in iron, as defined in Equation (18),

$$R_d\left[\frac{1}{cm^3 \cdot s}\right] = \phi\left[\frac{1}{cm^2 \cdot s}\right]\sigma_d\left[cm^2\right]N\left[\frac{1}{cm^3}\right], \tag{18}$$

where $\phi = 3.5 \times 10^{15}\left[neutron / cm^2 / s\right]$, $\sigma_d = 192\ barn = 1.92 \times 10^{-22}\ cm^2$, and $N = 8 \times 10^{22} / cm^3$. The displacement cross section for iron under neutron irradiation in HFIR has a low value due to the incorporation of thermal neutrons in the neutron flux energy spectrum, which in general do not cause direct displacements through elastic scattering.

Fortunately, there is another way to calculate the displacement rate, as defined in Equation (19),

$$R_d\left[\frac{1}{cm^3 \cdot s}\right] = \lambda\left[\frac{PKA}{cm^3 \cdot s}\right]P_d\left[\frac{displacements}{PKA}\right], \tag{19}$$

where the displacements per PKA can be computed by the Lindhard model and the PKA spectrum as mentioned before.

Combining Equations (18) and (19) yields the PKA production rate, $1.72 \times 10^{15}\left[PKA / cm^3 / s\right]$. Thus, the intra-cascade cluster production probabilities can be obtained by multiplying the values in the third column of Table 2 with PKA production rate, and these values are noted in the last column of Table 2.

Table 2. Intra-cascade cluster production probabilities P_i in 1/PKA.

Cluster Type	Cluster Size	Production probability (1/PKA)	Production rate (1/cm^3/s)
Interstitial Clusters	-20	0.0024	4.13×10^{12}
	-16	0.0048	8.26×10^{12}
	-12	0.0064	1.10×10^{13}
	-9	0.0144	2.48×10^{13}
	-8	0.0183	3.15×10^{13}
	-7	0.0413	7.10×10^{13}
	-6	0.0572	9.84×10^{13}
	-5	0.0838	1.44×10^{14}
	-4	0.1165	2.00×10^{14}
	-3	0.1794	3.08×10^{14}
	-2	0.3539	6.09×10^{14}
	-1	1.1215	1.93×10^{15}
Vacancy Clusters	1	1.8264	3.14×10^{15}
	2	0.5005	8.61×10^{14}
	3	0.1782	3.06×10^{14}
	4	0.1073	1.84×10^{14}
	5	0.0602	1.04×10^{14}
	9	0.0302	5.20×10^{13}

In the rate theory based reaction-diffusion cluster dynamics model, the mobile species determine the complication of the binary reactions, and correspondingly, the computational cost. In many previous reaction theory based models [28, 29, 41, 42], only V, SIA and di-SIA have been considered as mobile in order to simplify the model. However, experimental observations [52] have shown that interstitial loops containing a few to several hundreds of SIAs in BCC iron are mobile with nearly size-independent migration energies. These SIA clusters are predicted to be even more mobile in MD simulations [43, 50, 51, 53-56], in which the activation energies of the mobile SIA clusters are close to or even lower than the single SIA migration energy. Xu [40] et al., summarized the currently available expressions for the migration energies and the diffusivity pre-factors of interstitial clusters as a function of cluster size from MD

simulations, ab initio calculations and TEM experimental observations. Xu proposed a mobility parameter set for the prediction of microstructural evolution in krypton-ion irradiated molybdenum based on the simulations and experimental observation results available in the literature for BCC iron. In the present model of neutron irradiation of iron, all of the interstitial loops are considered mobile. Table 3 lists the set of mobility data chosen on an empirical basis by considering the various studies used for the modeling of Fe-a samples (high purity). The selected parameter set is quite similar to that chosen by Xu in a recent study [40].

Table 3. Mobility set for interstitial clusters/loops and single vacancy for the modeling of neutron irradiated Fe-a samples.

Cluster	V	$I - I_7$	I_8	I_9	I_{10}	I_{11}	I_{12}	I_{13}	I_{14}	I_{15}	$I_{n>15}$
E_m (eV)	0.75	0.34	0.45	0.50	0.55	0.65	0.75	0.80	0.9	0.95	1.1
D_0(nm^2/s)	1.37×10^{11}					$1.37\times10^{11}/n$					$1.37\times10^{11}n^{-0.7}$

The energetics and expressions of V_n and I_n transitions (e.g., cluster dissolution) are consistent in almost all of the cluster dynamic models. The binding energies of SIA and single vacancy to the small clusters (up to 4) are obtained using ab initio calculations by Fu et al. [57]. For larger interstitial and vacancy clusters, an extrapolation method was used to calculate the required binding energies, based on the MD simulations of Soneda et al., [58], indicating that the formation energies of interstitial and vacancy clusters follow a 2/3 power law with increasing number of defects in the cluster.

Irradiation hardening model

As mentioned in the introduction, precise estimation of the increase of the yield strength induced by neutron irradiation relies on the establishment of a reliable relationship between the irradiation-induced defect density and the resolved shear stress required to move the dislocation through an obstacle field. The dispersed barrier-hardening model is used here to predict the increase of the yield strength. Equation (1) is the classical expression of the Orowan model and various corrections of this equation have been proposed, including (i) introducing the Kocks/Foreman and Martin statistical factor to convert the planar interparticle spacing to an effective interparticle spacing (i.e., 1.2 times the original value) and then allowing for finite particle size; (ii) using more refined estimates of the line tension; (iii) allowing for mutual interaction of the bowed-out segments of the dislocation on either side of the particle. Combing all these modifications for a set of particles of diameter *d*, Kelly [11] proposed the modified Orowan equation,

$$\Delta\tau_s = \alpha \frac{0.83\mu b}{\left[(Nd)^{-0.5} - d\right]} \frac{\ln(d/r_0)}{2\pi(1-\nu)^{0.5}}. \tag{20}$$

The α factor has been included in Eq. (20) to indicate its correspondence with Equation (1). In Equation (20), μ is the shear modulus, which is 82 GPa for BCC iron, and *b* is the magnitude of the a/2<1 1 1> Burgers vector. *N* and *d* are the number density and

diameter of the defect clusters. r_0 is the dislocation core radius, which is defined as the distance below which linear elasticity does not hold. The value of r_0 is generally taken to be several times the Burgers vectors (*b*~5*b*). ν is the Poisson ratio, which is approximately 1/3 for iron.

The obstacle strength is given by the factor α. This value can vary between zero and one, and is strongly dependent on the types of defects. In pure iron under neutron irradiation, dislocation loops and nanovoids are the only two defect populations observed. All of the samples were fully annealed before being placed in the irradiation environment, therefore, it is reasonable to assume that the density of dislocations from the initial dislocation network is low compared to the density of prismatic loops created under neutron irradiation, and that its contribution to the radiation-induced yield stress change, or hardening, is negligible. In the present work, the increase of yield strength of the iron samples after neutron irradiation is exclusively ascribed to the existence of irradiation-produced vacancy cluster and interstitial loops, of which the α values need to be identified.

The strength factor α has been studied extensively using both experimental and modeling approaches for both voids and loops [19,59-63]. The hardening-contribution due to visible loops in vanadium alloys has been estimated by utilizing Equation (1) in combination with TEM measured loop density and size, giving α values in the range from 0.40 to 0.50. Rice and Zinkle [19] also indicate that α is a function of temperature. Similar experiments performed by Lambrecht and co-authors [59] show that α values for dislocation loops can be as high as 0.7 in neutron irradiated pure iron but this value varies for different alloys. By combining PAS measurements with the tensile tests, they concluded that very small vacancy clusters contribute little to the hardening. Meanwhile, the strengthening effect of voids in iron has been investigated theoretically by many researchers [60-62], and these studies consistently indicate that voids are strong obstacles to dislocation motion. In the literature, α is most often assumed to be a constant (e.g., 0.1 for loops and 0.16 for voids [63]) to describe the overall impeding resistance of the defects to the dislocation motion. However, it is reasonable to assume that the strengthening factor α should be a function of the defect size, defect type, temperature, and possibly strain rate. Here, we assume that α exclusively depends on the size of the defects since the tensile test conditions were the same. The exact functional form is unknown, but certain properties of the function are known. The strength of the defects should presumably monotonically increase with their size. It should reach a maximum value of unity for large defect clusters, and as the defect size approaches zero, it should reach a minimum value of zero. One such simple expression is thus

$$\alpha = 1 - \exp\left[-\left(\frac{d}{d_{ref}} \right)^n \right], \tag{21}$$

where d_{ref} is a reference defect size and n is the strength sensitivity to the defect size, which are further constrained such that α is 0.1 for a loop size of 2 nm and 0.3 for a void size of 2 nm. The choice of these limits is based on the commonly used values of α for loops and voids [63] and the comparison of the modeling results and experimental measurements. MD simulations [61, 62] reveal that voids are strong

obstacles when the size is larger than 2 nm. Moreover, loops act as slightly weaker obstacles compared to voids [63]. Consequently, 4 nm is assigned to d_{ref} and n is set equal to 1.5 and 3.3 for voids and loops, respectively. Figure 2 shows the calculated strength factor, α, as a function of the diameter of interstitial and vacancy clusters, respectively, based on Equation (21).

Finally, we note that the increase of the critical shear stress cannot be directly compared to the experimental measurement. The Taylor factor (3.06 for non-textured BCC and FCC metals [64]) is routinely used to correlate the shear stress increase with the measured applied stress, which correspondingly has the form of

$$\Delta\sigma_y = M\Delta\tau_s, \tag{22}$$

where M is the Taylor factor.

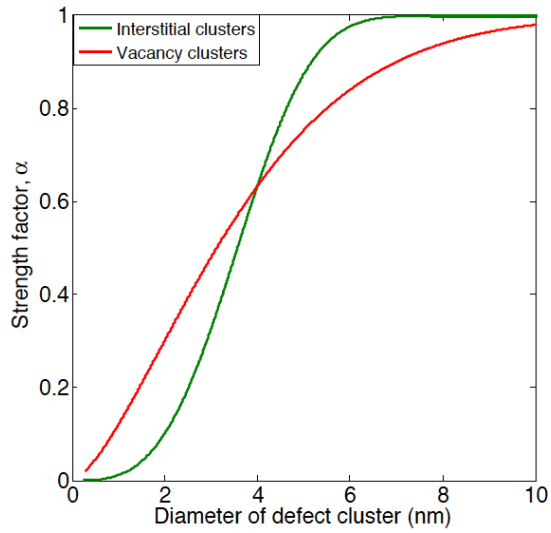

Figure 2. Strength factor, α, as a function of the diameter of an interstitial (dislocation loop) or vacancy (cavity) cluster, respectively.

RESULTS

<u>Predictions of vacancy and interstitial clusters produced in iron samples under neutron irradiation</u>

Following the cluster dynamics model and parameters introduced in Section 3.1, the vacancy and interstitial cluster distributions have been simulated for the pure iron samples (Fe-a) under neutron irradiation. Note that the irradiation temperature during the irradiation of these samples was not constant due to placement variation within the hydraulic tube facility. A temperature gradient exists, for which the temperature varies from 333K to 373K, consistent with the experimental conditions described in Reference [18]. Therefore, the simulation results presented here have been performed at these two limiting temperatures. Figure 3 presents modeling results of the vacancy and interstitial cluster distributions as a function of irradiation dose. It can be seen that

interstitials undergo significant clustering at these doses and temperatures, while vacancies do not, which reflects that the interstitials are much more mobile than vacancies. By comparing Figure 3 (a) and (b), one can see that clustering of both interstitials and vacancies is larger at the slightly higher temperature at 373 K. As mentioned in the introduction, it is crucial to have precise predictions of interstitial and vacancy cluster distribution to determine the irradiation hardening. Thus the current cluster dynamics modeling results must be verified by experimental measurements before being used within the hardening model.

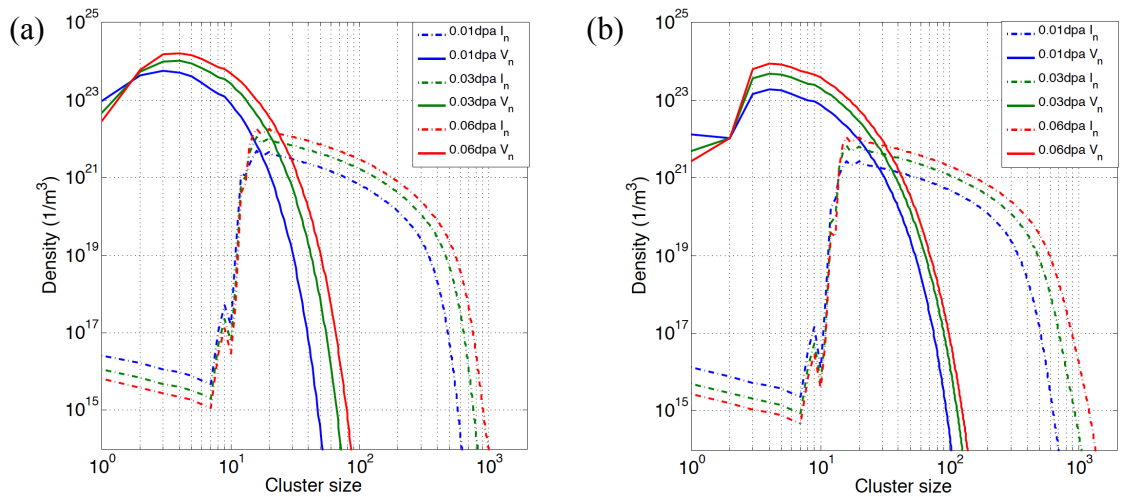

Figure 3. Model predicted volumetric density of interstitial and vacancy clusters plotted as a function of cluster size (n, # of point defects in the cluster) at (a) 333K and (b) 373K for Fe-a samples following selected radiation doses (0.01 dpa, 0.03 dpa, and 0.06 dpa).

Eldrup et al., [36] used PAS to obtain information on the vacancy cluster populations in pure iron (Fe-a) after these same neutron irradiation conditions. In the quantitative analysis, the measured lifetime spectra for the irradiated Fe-a samples were resolved into five lifetime components, four of which have fixed lifetimes: 200, 300, 400, and 500 ps, equivalent to three dimensional vacancy clusters with a size of about 0.35, 0.54, 0.73, and > 1.0 nm in diameter, respectively. The application of the trapping model to the measured positron lifetime spectra was used to obtain the density of different defect clusters, providing a rough size distribution of vacancy clusters for Fe-a under various irradiation conditions, shown in Figure 4. The total density of vacancy clusters for each irradiation dose level can thus be obtained by summing the concentrations of different defects, indicated in Figure 5. The output from the model predictions, similar to that shown in Figure 3 but at an appropriate dose level, can be easily analyzed to extract the quantities that are acquired in the experiments so that direct comparisons can be drawn between the modeling predictions and the PAS measurement. For example, the total volumetric density of vacancy clusters can be obtained by summing over different defects, and the size distribution can be obtained by binning the defects into various size intervals and summing the volumetric densities within each bin. In Figure 4, the modeling results of the vacancy cluster size distributions at 333K and 373K are plotted together with the PAS measurements for three different irradiation doses of 0.0001, 0.0009 and 0.009 dpa. Generally, the modeling results show a similar trend of

increasing density of increasing cluster sizes with increasing radiation dose, as the experimental measurements. For the neutron irradiation doses of 0.0001 dpa and 0.0009 dpa, the PAS experimental analysis indicates that most of the vacancy clusters have a size less than 3.5 nm and the densities decrease with increasing sizes. The models reproduce these features except the modeling predictions at 0.0009 dpa at 373K, for which the vacancy clusters of intermediate sizes have a slightly larger volumetric density. When the neutron dose increases to 0.009 dpa, the PAS results show that the vacancy clusters with diameters in a range of 0.35-0.54 nm are dominant in the measured positron lifetime spectra, which is also in good agreement with the model predictions. Figure 5 shows a comparison of the total density of vacancy clusters obtained from the PAS measurements with the modeling predictions at the two limiting temperatures. Overall, the modeling predictions at these two temperatures bracket the PAS measurements, and are in quite good agreement when considering the uncertainty within the experimental measurements.

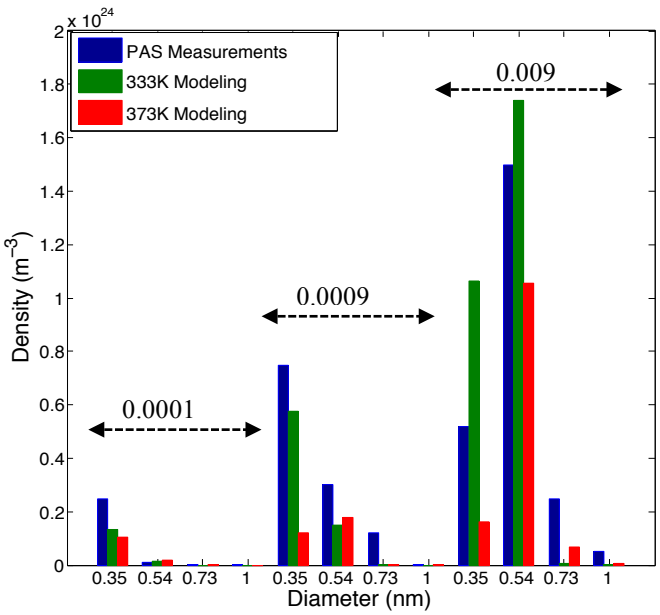

Figure 4. Comparison of modeling predictions and experimental measurements of size distribution of vacancy clusters in Fe-a at different irradiation dose levels of 0.0001, 0.0009 and 0.009 dpa.

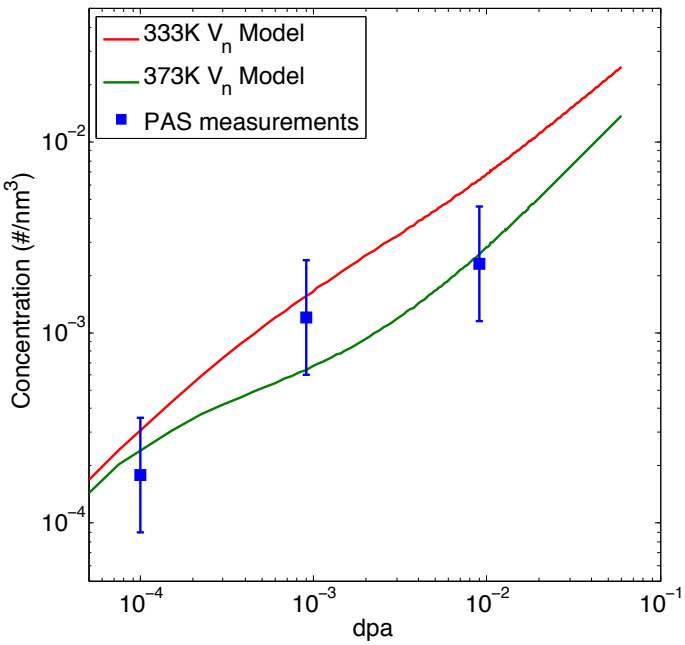

Figure 5. Comparison of modeling predictions and PAS measurements of the total density of vacancy clusters in Fe-a at different irradiation doses.

The PAS thus provide a comparison and verification of the vacancy cluster distribution predicted by the cluster dynamic model based on reaction-diffusion rate theory. As well, it is important to validate the modeling prediction of the interstitial cluster distribution. Reference [36] describes the results of a TEM investigation on the neutron irradiated Fe-a samples performed to characterize the density of the interstitial type dislocation loops. It is important to note that not all of the interstitial clusters, but only those with a diameter exceeding the TEM resolution limit, can be observed by TEM. Furthermore, not all dislocation loops will be resolvable in the TEM due to the ***g.b*** invisibility criteria [65]. The resolution limit in such TEM experiments varies slightly with material condition as well as TEM operating conditions, but is generally in the range of 1.0-1.6 nm. In BCC iron, a 1.4 nm diameter corresponds to a 32-member interstitial cluster (I_{32}) of 2-D planar shape, and a 1.6 nm diameter corresponds to I_{42}. This implies that the comparison of the modeling results and the experimental observations will be sensitive to the choice of the TEM resolution limit. Given the overall interstitial cluster distributions shown in Figure 3, a straightforward calculation is performed to obtain the total density of the visible interstitial clusters by summing up the density of the defect clusters with sizes that exceed the TEM resolution limit. Figure 6 (a) lists the TEM observations and the modeling results at two different neutron irradiation temperatures for four different TEM resolution limits. Although there are some discrepancies between the modeling and TEM measurements, the order of the magnitude of the interstitial cluster densities are generally comparable, and within the experimental error [36]. It is

noted that the lower the TEM resolution limit (larger diameter for the smallest observable loop), the closer the experimental measurements and the modeling results are. Also, the modeling predictions at 373 K agree slightly better with the experimental observations. Another important parameter for the validation of the developed model is the average size of dislocation loop, which is obtained from weighted average of visible interstitial clusters. The comparison between modeling predictions and experimental observations [66] is shown in Figure 6 (b) and a quite good agreement is acquired.

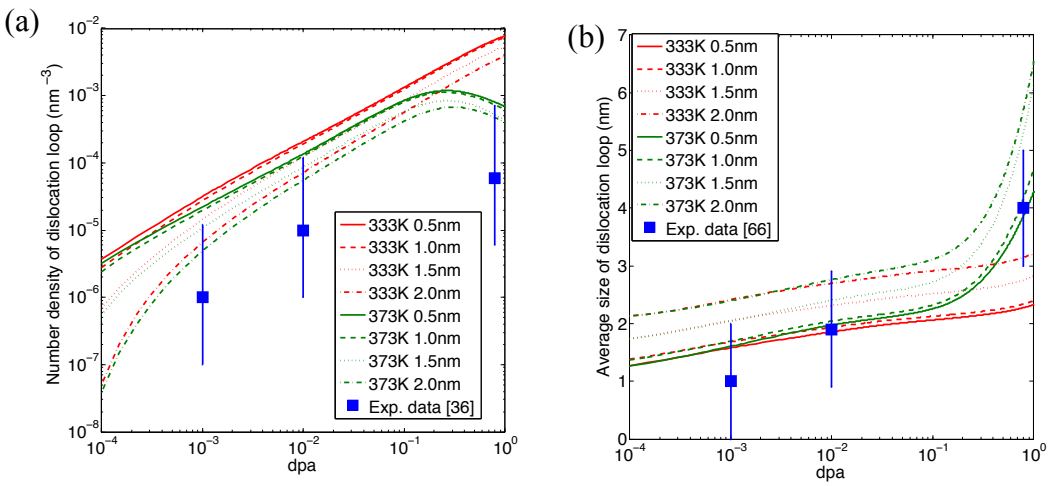

Figure 6. Cluster dynamics modeling predictions of (a) interstitial-type dislocation loop density and (b) average size of the visible dislocation loop for 4 different TEM resolution limits (0.5 nm, 1.0 nm, 1.5 nm, and 2.0 nm) at two different neutron irradiation temperatures for the Fe-a samples, as compared to the TEM observations of Reference [36, 66].

Based on these comparisons, we can conclude that our cluster dynamic model is providing acceptable predictions of the vacancy and interstitial clusters distributions produced in the Fe-a samples exposed to neutron irradiation in HFIR.

For the Fe-b samples, it is most likely inappropriate to directly use the modeling results obtained for the Fe-a samples due to differences in the impurity content of these two samples, as listed in Table 1. It is well known that the existence of impurities changes the kinetics and energetics of the defect clusters. In a recent study, Hu et al., [31] showed the influence of impurities on helium-point defect interactions by comparing the thermal desorption spectra of two different batches of single crystalline iron samples. Changes to the migration energies and binding energies of some important small clusters were observed. Note that the discrepancies between the two batches of samples are quite similar to the current Fe-a and Fe-b samples, therefore, it is reasonable to apply a similar change in the mobility parameter set in order to simulate the neutron irradiated defect microstructure of the sample Fe-b. Table 4 lists the optimized migration energies of interstitial clusters/loops and single vacancy used to predict the defect distribution of the Fe-b samples after neutron irradiation.

Table 4. Mobility set for interstitial clusters/loops and single vacancy for the modeling of neutron irradiated Fe-b samples.

Cluster	V	I	I_2	I_3	I_4	I_5	I_6	I_7	$I_{n>8}$
E_m (eV)	0.85	0.38	0.45	0.50	0.55	0.65	0.75	0.85	1.2
D_0(nm^2/s)	1.37×10^{11}				$1.37\times10^{11}/n$				$1.37\times10^{11}n^{-0.7}$

Unfortunately, detailed experimental characterization results of the neutron irradiated Fe-b samples are not available, which limits the ability to directly compare and validate the modeling results. Here, we show the modeling predictions of the interstitial and vacancy clusters as a function of irradiation dose levels at the two-irradiation temperatures of 333 and 373 K, which are subsequently used to compute the increase of yield stresses. However, as mentioned in the introduction, tensile test data does exist for the Fe-b samples, and will be compared to the model predictions. Figure 7 shows the model predictions of the vacancy and interstitial clusters using the mobility parameter set listed in Table 4. The results have similar features with those of the Fe-a samples shown in Figure 3. The most significant difference is that the predicted interstitial cluster population in Fe-b has a smaller size distribution due to the slightly lower assumed mobility of interstitials as a result of the higher impurity concentration in this sample.

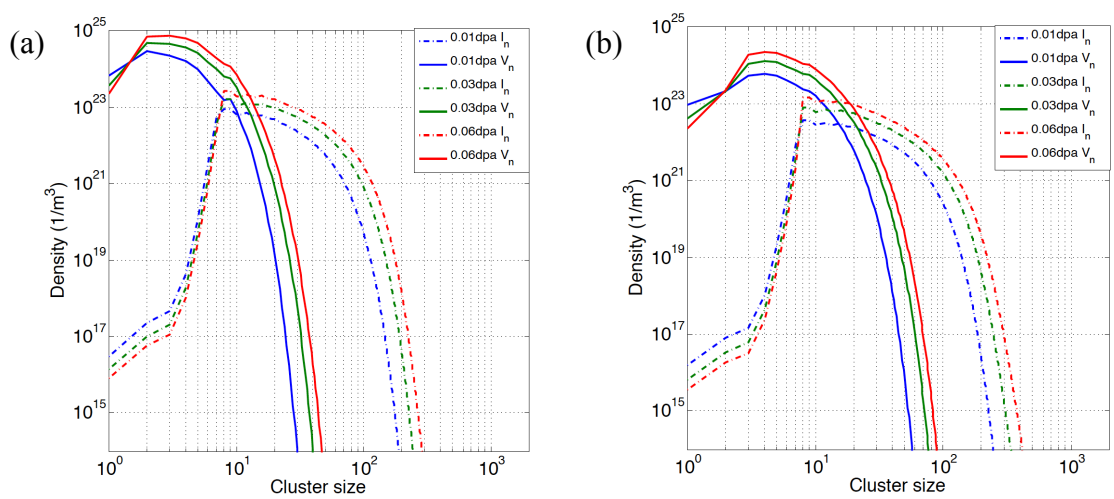

Figure 7. Model predicted volumetric density of interstitial and vacancy clusters as a function of cluster size at (a) 333K and (b) 373K for Fe-b samples following selected radiation doses (0.01 dpa, 0.03 dpa, and 0.06 dpa).

Irradiation hardening prediction

As described in Section 3.2, the increase of yield strength is computed by Equation (20), for which all of the necessary parameters have been determined. Note that this equation is only valid for one specific defect cluster with a fixed diameter. However, as shown in Figure 3 and 7, the microstructure of the neutron-irradiated iron involves a continuous size distribution of both interstitial and vacancy clusters. In order to assess the hardening of a true irradiated microstructure, we must account for obstacles of different types, sizes and number densities. In most mechanistic models, the total yield strength increase under irradiation is obtained as the superposition of the different defects. This superposition can be performed using either a linear or a root-sum-square of the individual components. It is emphasized here that neither of these superposition laws is fully supported by any clear physical motivation. In the present work, interstitial loops and nanovoids are assumed to be the only two defect populations responsible for the radiation-induced hardening increment, and the total hardening increases will be given by the square root of the two contributions, as both loops and voids are assumed to be relatively strong obstacles, of similar strength, as suggested in Reference [27].

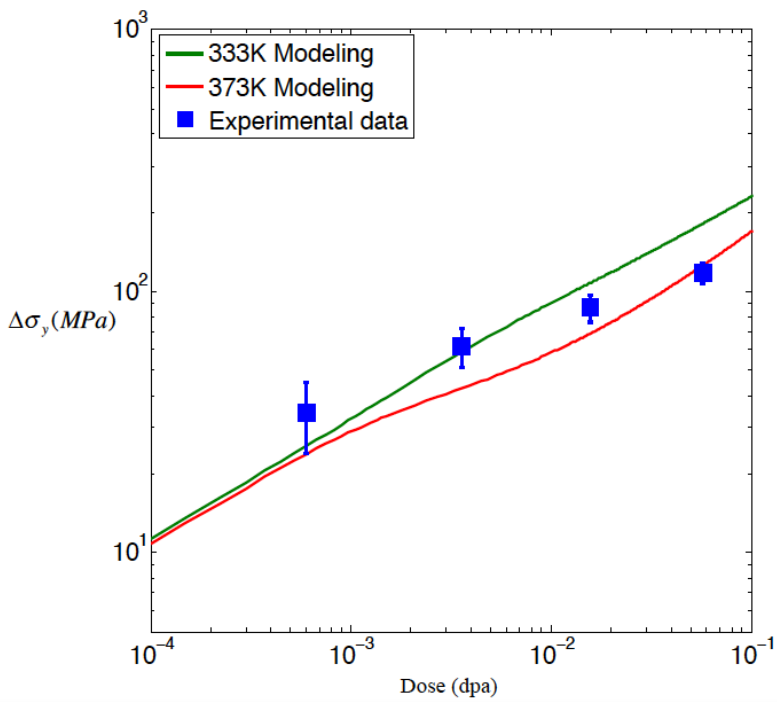

Figure 8. Hardening model predictions for the Fe-a sample at 333 and 373 K irradiation, as a function of dose (green and red lines, respectively) versus experimentally measured tensile data from Reference [18].

For the Fe-a high purity iron samples, the incorporation of the cluster dynamic modeling results, as shown in Figure 3, within Equations (20)-(22) leads to the prediction of yield strength increase. Figure 8 shows the irradiation hardening modeling results and the experimentally measured tensile data of yield strength increase for the Fe-a samples. The modeling results successfully bracket the measured yield strength increases at 0.0006 dpa, 0.0036 dpa, 0.0157 dpa, and 0.0574 dpa. The measured yield strength

increases are similar in the lower dose regime (less than 10^{-3} dpa) as the modeling predictions at 333 K and 373 K. The 40 K difference in temperature does not impact the modeling prediction significantly until the neutron irradiation dose reaches slightly higher values, which is consistent with the loop and vacancy distributions predicted by the cluster dynamic model. In previous irradiation hardening studies, a simple power-law expression, $\Delta\sigma_y = h\phi^n$, where ϕ is the radiation dose level, and *h* is a pre-factor, has been used to describe the hardening behavior in the low dose regime [12, 37]. At low doses below about 0.01 dpa, the exponent *n* has been measured to be about ½ for many metals [8, 20, 37, 67]. By applying this expression to the current model predictions, the exponent *n* can be determined to be 0.44, quite close to the previous values.

Table 5. Modeling results of the yield strength increase at two neutron irradiation temperatures and the tensile test measurements for two neutron irradiation conditions for Fe-b iron samples.

Dose (dpa)	0.0001	0.001
Tensile Tests (MPa)	13.2±5.5	27.5±5.5
333K (Model, MPa)	11.42	32.42
373K (Model, MPa)	10.94	29.06

The Fe-b samples contained higher level of impurities, which have been assumed to reduce the mobility of the mobile species and influence the predicted defect cluster distributions. The modeling predictions of the yield strength increase for the neutron irradiation doses of 0.1 and 1 mdpa are shown in Table 5 along with the experimental measurements. The model slightly underestimates the increase of the yield strength at 0.0001 dpa and slightly overestimates it at 0.001dpa. But, overall, the predicted yield strength increases at 333K and 373K is well matched with the measured tensile test results, and are certainly within the range of the estimated measurement error. The limited experimental data obtained on the Fe-b samples prevents further comparison with the model predictions.

It is emphasized that the current modeling results and experimental comparison are focused on the low dose and low irradiation temperature regime. Overall, the experimental measurements and the modeling predictions are in good agreement within the range of experimental uncertainty.

DISCUSSION

Irradiation hardening is an extremely complicated problem resulting from the complex microstructures, which develop under neutron irradiation. In the present study, the dispersed barrier-hardening model provides some insights into the relationship between the yield strength increase and the primary microstructure evolution of two high purity iron samples under neutron irradiation. However, this simple model is not sufficient to

capture the contribution from every possible defect and to reveal all underlying mechanisms. As well, some uncertainties exist in the model, and it is necessary to evaluate these key factors, e.g., the dislocation core radius, the choice of the superposition law, the applicability of the model in the high dose regime, etc., which might significantly impact the results.

The value for the dislocation core radius, r_0, shown in Equation (20), of 2b has been used in this work, and provides the best agreement between the experimental data and modeling predictions. However, the dislocation core radius has no recommended theoretical value, and is typically discussed with values from 1b to 5b [63], which makes it important to indicate the susceptibility of the predicted yield strength increase to r_0. Here, the modeling case of high purity iron under neutron irradiation at 333K is taken as an example to show how the model predictions of yield strength increase vary when using different r_0, as shown in Figure 9. When the radiation dose is lower than 7 mdpa, the predicted yield strength increase is almost independent of the dislocation core radius. The modeling results using r_0=2b are smaller than those using 3b and 4b when the radiation dose begins to exceed 7 mdpa. By 0.1 dpa, the predicted yield strength increase using a cut-off radius of 2b is approximately 25% smaller than the value using either 3b or 4b. However, overall, the variation of dislocation cutoff radius, r_0 does not significantly change the model predictions of the yield strength increase within the studied dose range.

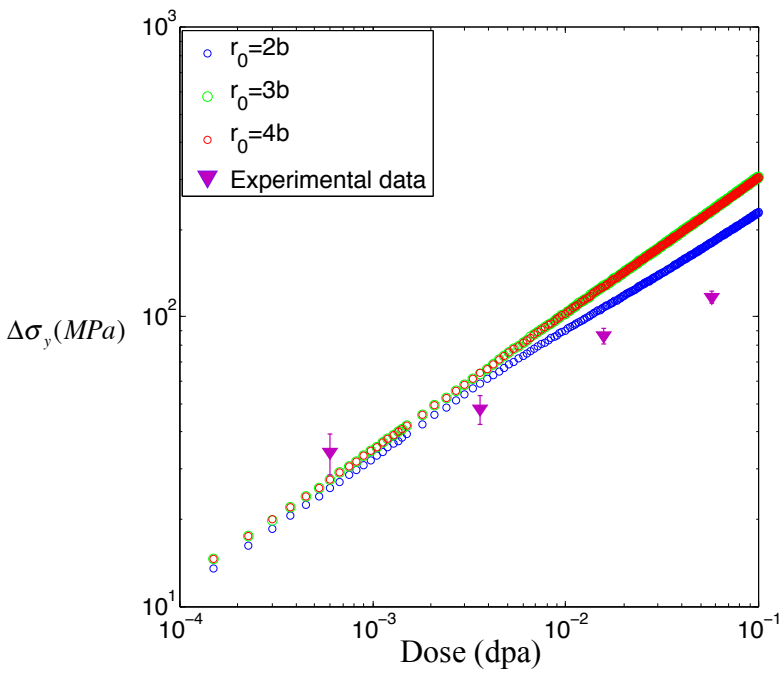

Figure 9. Model predictions of the yield strength increase of the Fe-a iron samples following neutron irradiation at 333 K, as a function of dislocation core radius sets as compared with the experimental measurements from Reference [18].

In Section 4.2, the root-sum-square superposition law was used to integrate the contributions from each interstitial cluster. Since the interstitials have long-range strain fields, the interactions between them are strong and it is possible to argue that a linear

superposition law might be more appropriate. Figure 10 shows a comparison of the model predictions resulting from these two different superposition laws for the neutron irradiated Fe-a iron sample at 333 K. It is obvious that the use of a linear superposition law overestimates the yield strength increase at irradiation doses above about 5 mdpa. Thus, given the good agreement between the predicted vacancy and interstitial cluster populations with the experimental PAS and TEM characterization discussed in Section 4.1, we conclude that the root-sum-square superposition law is most appropriate to predict the yield strength increases in the present study, which is consistent with the analysis by Lambrecht [59].

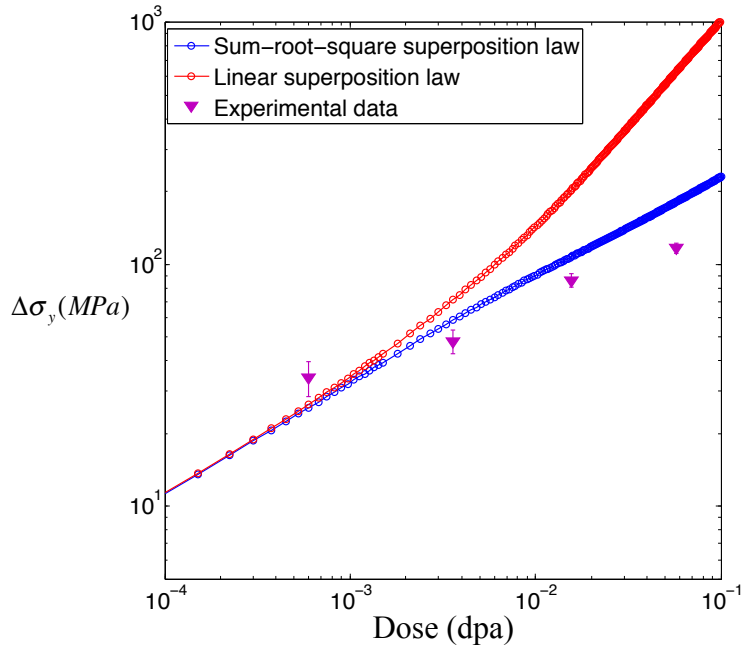

Figure 10. Model predictions of the yield strength increase for root sum square versus linear superposition laws applied to simulations of the neutron irradiated Fe-a iron sample at 333 K as compared with the experimental measurements from Reference [18].

As mentioned in Section 4.2, the present model is focused on the low irradiation dose regime, and thus it is not entirely clear the extent to which the current model is applicable to predicting higher radiation dose microstructure evolution and yield strength changes. Neutron irradiation continuously introduces point defects and defect clusters, which undergo diffusion-driven evolution dictated by the evolving radiation-damaged microstructure. As shown in Figures 3, 4 and 7, the model predicts that the vacancy and interstitial cluster size distribution continues to grow to larger size with increasing irradiation dose. Consequently, the average size and concentration of the vacancy and interstitial clusters are both increasing. However, this process will not continue forever. Equilibrium will be achieved at some point, when the collective generation and annihilation rates of vacancy and interstitial clusters equilibrate. Therefore, a saturation of the average size and concentration of the defect clusters can be expected to occur. Experimentally, a tendency towards saturation is observed when considering the mechanical property changes, such as yield strength increases [7, 18,

68], but not observed for dimensional stability such as swelling [69, 70]. However, the experimental data at high neutron exposure conditions is quite limited and there does not currently exist a consensus with respect to the tendency to saturate the radiation-defect microstructure or the resulting property changes.

However, given that the increase of yield strength is ascribed to the radiation-produced defect clusters, and the previous paragraph argues for a saturation of the defect cluster evolution; the saturation in radiation-induced defect clusters will also produce a saturation of the yield strength increase. Here, the modeling example of the low purity, Fe-b sample irradiated at 333K is taken as an example to show the model predictions of higher dose behavior, as shown in Figure 11. The model predicts that $\Delta\sigma_y$ begins to saturate at a dose of about 2 dpa, with complete saturation by about 20 dpa. However, tensile tests indicate that the irradiation dose for this transition is around 0.05 dpa [18], much less than the model prediction. Moreover, the saturation value of $\Delta\sigma_y$ predicted by the cluster dynamics model is around 10^4 MPa, which is almost two orders of magnitude larger than the strength increase experimentally measured in Reference [18].

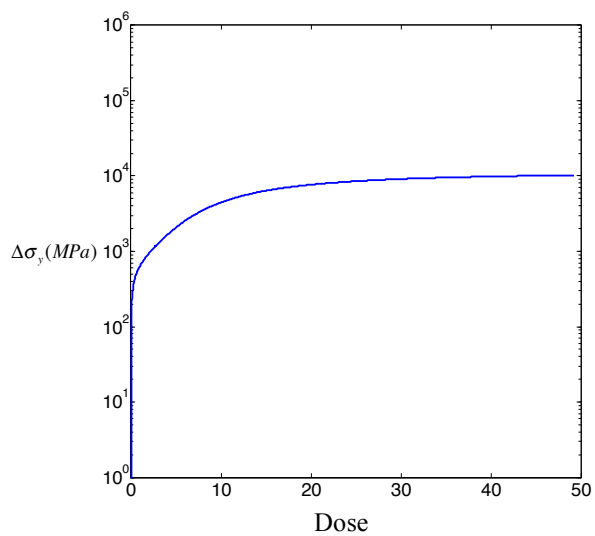

Figure 11. Model prediction of the yield strength increase as a function of irradiation dose for the Fe-b sample irradiated at 333 K.

We presume that this significant over-prediction of the model in the high dose regime is due to the complexity of the radiation-damaged microstructure and the corresponding irradiation hardening combined with the simplifying assumptions used in the model. For instance, plastic instability at yield and dislocation channel deformation can influence the transition from the low to high dose regime [18, 71, 72], and are not explicitly included in the dispersed barrier-hardening model. Additionally, it is clear that a spatially uniform defect cluster distribution, as predicted by a mean-field reaction-diffusion cluster dynamics model will not be reliable at high doses. Numerous experiment have shown the formation of spatially correlated dislocation loop microstructures in the form of rafts [36, 66], which begin to be observed at dose levels on the order of 1 dpa. Likewise, MD simulations [73, 74] indicate that as defect cluster volume fraction increases (and the inter-defect spacing decreases) at high radiation

doses, it is more likely that the defects in a newly produced displacement cascade will react with the existing clusters at the expense of new clusters, essentially promoting recombination or clustering reactions that marks a steady-state behavior and limits nucleation of new defect clusters. These effects are not included in the current model, and thus it is easy to see how the cluster dynamics model could over-estimate the defect cluster populations at high dose. Consequently, the predicted yield strength increase is over-estimated. Therefore, it is emphasized here that the current model is only applicable in the low dose regime prior to the occurrence of significant spatial correlation effects on the radiation-induced defect cluster microstructure including cascade overlap. Future efforts must be dedicated to better defining the spatial distribution of radiation-induced microstructure required to parameterize and fit spatially-dependent models of neutron-induced damage evolution and property changes.

CONCLUSION

The neutron irradiation hardening behavior of two different, high purity polycrystalline iron samples at low dose and low irradiation temperature was modeled by applying a cluster dynamics model based on reaction-diffusion rate theory and the dispersed barrier hardening model. The evolution of the microstructure in terms of interstitial cluster type dislocation loops and nanovoids was simulated by the cluster dynamics model, of which the predictions of vacancy clusters and interstitial loops were validated by available PAS and TEM data, respectively. The dispersed barrier hardening model was used to correlate the defects with the increase of the yield strength by applying a continuous strength factor α as a function of defect size. Overall, the modeling results compare quite well to the experimental observations in the low dose regime, and provide insight into the underlying microstructure – property relationships. Furthermore, we have assessed the impact of the dislocation core radius and the model for superposition of the individual strengthening contributions within the dispersed barrier-hardening model, and find that a core radius of 2b and a root sum square superposition law are most appropriate for the current iron data at dose levels below 0.1 dpa. In considering the applicability of the model to predict radiation damage in the high dose regime, it is clear that spatially dependent modeling is required to accurately predict the saturation behavior of yield strength changes observed experimentally at higher dose levels. In the future, more experimental data, including the spatial distribution of defect clusters, are necessary to further verify the prediction of the defect cluster distributions obtained from the cluster dynamics model and to correctly model high dose phenomena.

ACKNOWLEDGE

The aid and technical insight of Kurt A. Terrani and Yutai Katoh at ORNL is gratefully acknowledged, as is financial support from the U.S. Department of Energy, Office of Fusion Energy Sciences under grant DE-FG02-04GR54750 and the U.S. Department of Energy, Office of Nuclear Energy's Nuclear Energy University Programs (NEUP).

REFERENCES

[1] E. E. Bloom, *J. Nucl. Mater.* **258-263** (1998) 7.
[2] K. L. Murty, *JOM* **53**(7) (2001) 8.
[3] G. R. Odette and G. E. Lucas, *JOM* **53**(7) (2001) 18.
[4] S. J. Zinkle and N. M. Ghoniem, *Fusion Eng. Des.* **51-52** (2000) 55.

[5] C. E. Ells and C. D. Williams, *Trans. JIM* **9** (1968) 214.
[6] R. P. Tucker and M. S. Wechsler, *Radiat. Eff.* **3** (1970) 73.
[7] M. J. Makin and F. J. Minter, *Acta Metall.* **8** (1960) 691.
[8] K. L. Murty and D. J. Oh, *Scr. Metall.* **17** (1983) 317.
[9] B. N. Singh, A. J. E. Foreman, and H. Trinkaus, *J. Nucl. Mater.* **249** (1997) 103.
[10] A. H. Cottrell and R. J. Stokes, *Proc. R. Soc. A* **233** (1955) 17.
[11] P. M. Kelly, *Int. Metal. Rev.* **18** (1973) 31.
[12] T. H. Blewitt, et al., *J. Nucl. Mater.* **2** (1960) 277.
[13] J. V. Sharp, *Phil. Mag.* **4** (1967) 77.
[14] J. V. Sharp, *Acta Metall.* **22** (1974) 449.
[15] Y. Dai, et al., *J. Nucl. Mater.* **212-215** (1994) 393.
[16] B. N. Singh, et al., *J. Nucl. Mater.* **299** (2001) 205.
[17] M. Victoria, et al., *J. Nucl. Mater.* **276** (2000) 114.
[18] T. S. Byun and K. Farrell, *J. Nucl. Mater.* **326** (2004) 86.
[19] P. M. Rice and S. J. Zinkle, *J. Nucl. Mater.* **258-263** (1998) 1414.
[20] A. Seeger, in: Proc. 2nd UN Int. Conf. on Peaceful Uses of Atomic Energy, Geneva, Sept. 1958, Vol. 6, p. 250.
[21] E. Orowan, *Nature* **149** (1942) 643.
[22] E. Orowan, Dislocations in Metals (AIME, New York, 1954) p. 131.
[23] A. Arsenlis, et al., *Phil. Mag.* **84** (2004) 3617.
[24] J. S. Robach, et al., *Phil. Mag.* **83** (2003) 955.
[25] U. F. Kocks, *Mater. Sci. Eng.* **27** (1977) 291.
[26] C. Pokor, et al., *J. Nucl. Mater.* **326** (2004) 30.
[27] C. Deo, et al., *J. Nucl. Mater.* **377** (2008) 136.
[28] D. H. Xu and B. D. Wirth, *Fusion Sci. Technol.* **56** (2009) 1064.
[29] D. H. Xu and B. D. Wirth, *J. Nucl. Mater.* **403** (2010) 184.
[30] D. Xu, X. Hu, and B. D. Wirth, *Appl. Phys. Lett.* **102** (2013) 011904.
[31] X. Hu, D. Xu, and B. D. Wirth, *J. Nucl. Mater.* **442** (2013) S649.
[32] X. Hu, Gas Diffusion in Metals: Fundamental Study of Helium-Point Defect Interactions in Iron and Kinetics of Hydrogen Desorption from Zirconium Hydride, Ph.D. Thesis, University of California, Berkeley, 2013
[33] T. Jourdan, et al., *J. Nucl. Mater.* **444** (2014) 298.
[34] S.J. Golubov, et al., *Philos, Mag. A* **81** (2001) 643.
[35] A. Gokhman and F. Bergner, *Radiat. Eff. Defects Solids* **165** (2010) 216.
[36] M. Eldrup, et al., *J. Nucl. Mater.* **307-311** (2002) 912.
[37] K. Farrell and T. S. Byun, *J. Nucl. Mater.* **318** (2003) 274.
[38] K. Farrell and T. S. Byun, Tensile properties of candidate SNS materials after irradiation in two neutron areas in the LANSCE accelerator, SNS/TR-211, Oak Ridge National Lab., January 2001.
[39] T. S. Byun, et al., *J. Nucl. Mater.* **303** (2002) 34.
[40] D. H. Xu, B. D. Wirth, M. M. Li, and M. A. Kirk, *Acta Mater.* **60** (2012) 4286.
[41] C. J. Ortiz, M. J. Caturla, C. C. Fu, and F. Willaime, *Phys. Rev. B* **75** (2007) 100102.
[42] C. J. Ortiz et al., *J. Appl. Phys*. **96** (2004) 4866.
[43] R. E. Stoller, et al., *J. Nucl. Mater.* **251** (1997) 49.
[44] R. E. Stoller, *J. Nucl. Mater*. **276** (2000) 22.
[45] W. K. Phythian, R. E. Stoller, et al., *J. Nucl. Mater.* **223** (1995) 245.
[46] R. E. Stoller, *J. Nucl. Mater.* **233-237** (1996) 999.
[47] L. R. Greenwood, R. K. Smither, SPECTER: Neutron Damage Calculations for Materials Irradiations, ANL/FPP-TM-197 Report, Argonne NL, January 1985;
[48] L. R. Greenwood, *J. Nucl. Mater*. **216** (1994) 29.

[49] M. T. Robinson. BNES nuclear fusion reactors. London: British Nuclear Energy Society; 1970.
[50] B. D. Wirth, G.R. Odette, R.E. Stoller, *MRS Soc. Symp. Proc.* **677** (2001) AA5.2.
[51] P. R. Monasterio, B. D. Wirth, and G. R. Odette, *J. Nucl. Mater.* **361** (2007) 127.
[52] K. Arakawa, et al., *Science* **318** (2007) 956.
[53] Yu.N. Osetsky, et al., *Phil. Mag.* **83** (2003) 61.
[54] C. C. Fu, et al., *Phys. Rev. Lett*. **92** (2004) 175503.
[55] B. D. Wirth, G. R. Odette, D. Maroudas, and G. E. Lucas, *J. Nucl. Mater.* **244** (1997) 185.
[56] J. Marian, et al., *Phys. Rev. B* **65** (2002) 144102.
[57] C. C. Fu and F. Willaime, *Phys. Rev. B* **72** (2005) 064117.
[58] N. Soneda, and T. Diaz de la Rubia. *Phil. Mag. A* **78** (1998) 995-1019.
[59] M. Lambrecht, et al., *J. Nucl. Mater.* **406** (2010) 84.
[60] R. O. Scattergood and D. J. Bacon, *Acta Mater.* **30** (1982) 1665.
[61] Yu.N. Osetsky and D. J. Bacon, *J. Nucl. Mater*. **323** (2003) 268.
[62] Yu.N. Osetsky and D. J. Bacon, *Phil. Mag.* **90** (2010) 945.
[63] G. S. Was. Fundamentals of Radiation Materials Science: Metals and Alloys, New York: Springer; 2007.
[64] R. E. Stoller and S. J. Zinkle, *J. Nucl. Mater.* **283-287** (2000) 349.
[65] M. Li, et al., *Phil. Mag.* **92** (2012) 2048.
[66] S. J. Zinkle and B. N. Singh, *J. Nucl. Mater.* **351** (2006) 269.
[67] A. Okada, et al., *J. Nucl. Mater.* **141-143** (1986) 907.
[68] J. E. Pawel, et al., *J. Nucl. Mater.* **239** (1996) 126.
[69] F. A. Garner, M. B. Toloczko, and B. H. Sencer, *J. Nucl. Mater.* **276** (2000) 123.
[70] S. J. Zinkle and G. S. Was, *Acta Mater.* **61** (2013) 735.
[71] S. J. Zinkle, *J. Nucl. Mater*. **150** (1987) 140.
[72] S. J. Zinkle, *Radiat. Eff. Defects Solids* **148** (1999) 447.
[73] H. L. Heinisch and B. N. Singh, *J. Nucl. Mater.* **271-272** (1999) 46.
[74] Y. Satoh, I. Ishida, T. Yoshiie, and M. Kiritani, *J. Nucl. Mater.* **155-157** (1988) 443.